A New Upwelling Radiance Distribution Camera System, NURADS

Kenneth J. Voss and Albert Chapin
University of Miami, Physics Department, Coral Gables, Fl. 33124
voss@physics.miami.edu

1) Introduction

Measurement of the upwelling radiance distribution in the ocean is difficult because of the number of observations required, the variability of the light field due to surface waves, and instrument self-shading, yet the upwelling radiance distribution is vitally important in ocean remote sensing. The radiance distribution is described by the collection of radiance data in all directions coming to a single point. At least two previous instruments have used single radiometers, swept over various directions in the zenith and azimuth directions (Tyler, 1960; Aas and Hojerslev, 1999). Tyler's Pend Oreille data set is still one of the fundamental tabulated data sets in the literature. The Aas and Hojerslev data set was used to develop a model of the angular variation of the radiance distribution. Both of these data sets were collected at a single central wavelength. Another method to measure the radiance distribution is the use of a fisheye camera system and a camera. This technique was first developed for in-water use by Smith, Austin, and Tyler (1970), using a photographic camera, and a photopic filter. This system allows the radiance distribution to be collected in two images (one upwelling - one downwelling), thus the entire radiance distribution can be obtained quickly, allowing rapid profiling if desired. The difficulty in this system was obtaining radiometric data from the photographic images. In addition, with a fisheye system, the lens radiometric effects must be taken into account, the main feature being lens-rolloff effects.

More recently a series of instruments have been built based on this fisheye technique, but using electro-optic cameras and remotely controlled spectral filter changers. The first of these systems, for use in the water (Voss, 1989) included CID electro-optic camera systems for both the upwelling and downwelling radiance distribution. This system consisted of three cans of instruments, with upwelling and downwelling systems in separate cans, along with a third can for the control electronics. The filter changer allowed selection of one of 4 spectral filters (25.4 mm interference filters), along with neutral density filters to adjust the overall sensitivity. These cameras were digitized with 8-bit frame grabbers, and did not have an intrinsically high dynamic range. But by coating the dome/window of the downwelling camera, and taking into account the lens system rolloff characteristics, the downwelling radiance distribution dynamic range could be accommodated. However, one useful characteristic of the CID architecture is that excess light in one pixel does not spread into neighboring pixels (bloom), thus while large dynamic ranges could not be measured because of the 8-bit data capture, it did not affect the rest of the image.

The next system in this series, RADSII(Voss and Chapin, 1992), was developed to take into account advantages in camera CCD development. This system used two cooled CCD cameras (512 x 512 pixels) and the same filter changer (with updated lens relay optics) to collect the radiance distribution. Both cameras, along with the control computer were housed in the same container. Along with these components, the system

had tilt/roll detectors, compass, and a multispectral upwelling/downwelling irradiance system (based on the MER 1032 [Biospherical Instruments] system). The size of the system was a cylinder approximately 0.4 m in diameter and 0.5 meter long. The system contained the camera control computer and hard drive, and communication with the system was by an RS-232 link. When on the surface an Ethernet link could be established, which allowed downloading data via an ftp transfer to the host computer on deck. While the instrument was in the water, a remote-control program (PCHost) allowed the operator to control the embedded computer functions. The data from the cameras was digitized with a 16 bit digitizer, however system noise reduced overall dynamic range to approximately 12 bits. This instrument was used during several experiments, in particular to gather surface upwelling radiance distribution data (Voss et al., 2003, Voss and Morel, 2004).

Because of the interest in the surface upwelling radiance we found that we were only using the upwelling radiance distribution from the system. To get accurate upwelling radiance distributions, without the effect of ship shadow, we floated the instrument away from the ship, which made it impossible to take upwelling/downwelling profiles or collect useful downwelling information. The size of the instrument, including the buoy to float it, caused a noticeable shadow effect in the images even in clear water (Doyle and Voss, 2000). This effect had been seen with the earlier instrument (Helliwell et al., 1990) and was smaller than before, however it was still a noticeable perturbation.

Because of instrument self-shading, and the desire to collect only upwelling radiance distribution data, the NURADS instrument was developed. The system still has a filter changer, embedded computer and hard drive, CCD camera, compass/tilt/roll sensor. However, by concentrating on only the upwelling radiance distribution and with advances in technology, this whole instrument package is only 0.25 m in diameter and 0.32 m long. With the reduction in size, the flotation can be reduced to a piece of foam, only 15 cm long, attached to the back of the instrument further reducing shadowing issues. The reduction in size greatly reduced the instrument self-shading issues, and several other improvements have helped the instrument provide more accurate upwelling radiance distribution data. This paper will describe this instrument, and provide some sample data from the instrument.

2) Fundamental NURADS instrument description

The instrument is based on an Apogee CCD array camera system (AP 260Ep) that uses the KAF 0261E CCD array. The camera housing includes the frame grabber electronics and interfaces directly with the embedded computer via the standard computer ECP parallel interface. The frame grabber digitizes the images at 16 bit resolution, the final system dynamic range will be discussed below. Included in the instrument is a 20 Gbyte 2.5” hard drive on which the camera images and auxiliary data is stored. There is an embedded Ez-Compass-3 that collects the tilt/roll/compass information and transfers it to the computer over a serial interface. This information is logged to the hard drive continuously during camera operation using the Logger program (Windmill Software, Ltd.). The system uses a fisheye adapter lens, designed for a Nikon Coolpix 950 camera (FC-E8), a custom lens relay system, and a Homeyer filter changer (MFW) (also

controlled over a serial interface) to form the fisheye camera image and provide spectral filtering. The filter changer uses 25.4 mm interference filters, and allows the selection of one of 6 spectral filters for the image. The embedded computer is controlled by a surface laptop computer by use of the Timbuktu remote control software. The link between the embedded computer and the laptop is via an Ethernet cable. While the data is still stored on the embedded computer hard drive, once data collection is completed the data on the hard drive can be extracted using the ftp method or with the Timbukto transfer commands.

Because of speed advances in the camera frame grabbing technology, enhanced sensitivity of the CCD array, and faster optics, a complete set of data (6 light images, 6 dark images, one with each spectral filter) in clear water, can be obtained in 2 minutes. The embedded computer controls the camera with a combination of MaxIM, Microsoft Excel, and Microsoft Basic programs. The typical operation of the camera is to run the system continually, acquiring data during the data collection period. By taking these multiple data sets, data can be excluded where the camera tilt/roll exceeds some threshold (usually 5 degrees), clouds are determined to be causing a problem with the incident light field, or some other temporary artifact is in the image. Multiple images are also averaged to reduce the effect of bright light rays due to the waves at the air-sea interface. In 30 minutes, 15 complete sets of data (approximately 90 Mbytes of data) can be acquired.

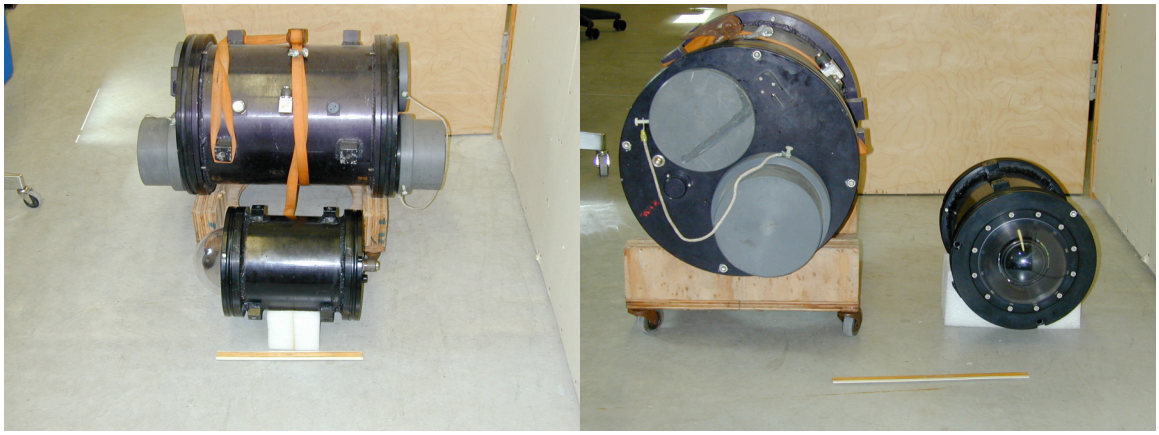

Figure 1) Left: Picture of NuRADS system (fore ground) with the older RADS-II system (background). Right: End-on picture of the NuRADS system (on right) and RADS-II system (on left). The new system is significantly smaller than the older system.

3) Characterization and Calibration

The method to characterize and calibrate the fish eye systems has been described earlier for the first RADS system (Voss and Zibordi, 1989). We will concentrate on the specifics results for this system.

The basic characteristics of the system relevant to the radiance distribution measurements are the lens system rolloff function, camera linearity, camera noise characteristics (dark

noise and readout noise), spectral calibration of filters/system. We will start with camera noise characteristics.

A) *Camera noise characteristics*

To see the background readout noise, and an indication of the dark noise level of the camera system, we averaged dark images (shutter closed) at several different integration times. The images were averaged, pixel-by-pixel to see if the variation was correlated with individual pixels, or was uniform across the array. Figure 2 shows a histogram of this pixel average (top) and the histogram for the standard deviation of the individual pixel averages (bottom). The pictures below show that the spread in integration times is very small for less than 2 sec, at 5 sec there is more variation. In terms of the standard deviation of the individual pixel averages, the average spread does not change significantly even at 5 sec integration. These two graphs imply that at longer integration times, there is some pixel-pixel variation in dark counts, but the noise does not increase. Thus subtracting a dark image from the data image is a better strategy then subtracting one overall average number. In our data collection we take a dark image at the appropriate integration time, and subtract (pixel by pixel) this image from the data image.

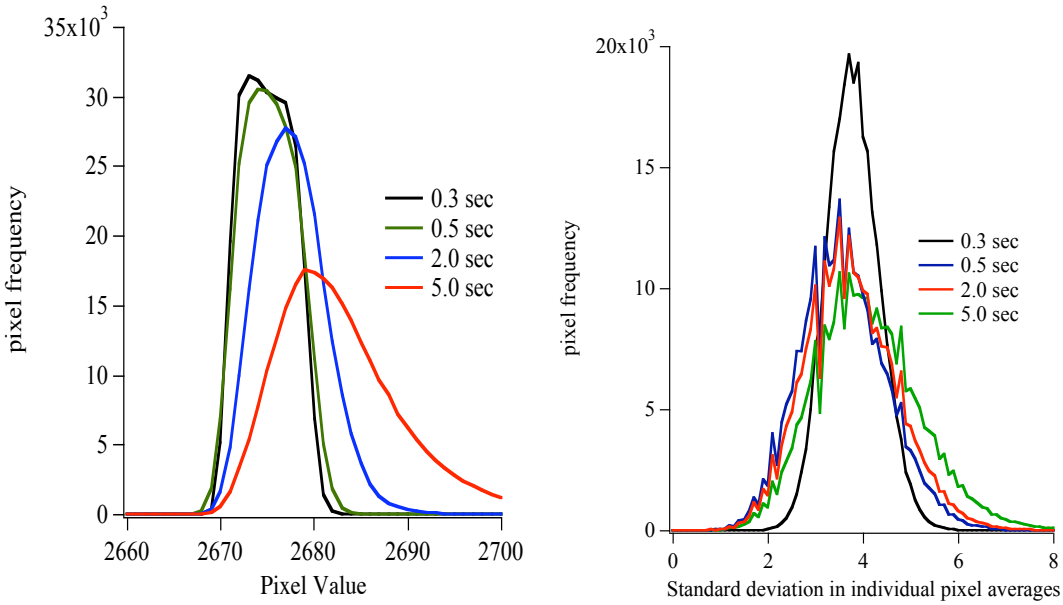

Figure 2) Dark noise data for the instrument. Left figure shows that the average pixel count of the dark/readout noise is approximately 2675 counts, and only increases when the integration time is greater than 2 seconds. Right figure shows that the standard deviation in the individual pixel averages is on the order of 4 counts.

These graphs also show that the intrinsic noise in the system is on the order of 4 counts, thus the system is easily operated as a 14 bit system and pixel averaging can increase the effective dynamic range of the system.

B) Camera linearity

The CCD camera is inherently a very linear device, and our system was no exception. This test will not be discussed in detail here, but it is similar to the results seen in the earlier system (Voss and Chapin, 1992).

C) Angular calibration

The natural projection of an ideal fisheye lens is a simple linear equation:

$$\theta = K\, r$$

where θ is the angle from nadir, r is the radial distance from the center of the image, and K is a calibration constant found through calibration.

We use a hemispherical dome as the window in the instrument. If the system is constructed, and adjusted properly, the first principal plane of the optical system will be at the center of curvature of the hemispherical dome. At this position, rays which make it through the lens system, will enter the dome perpendicular to the local dome surface, thus there will be little refraction, and the angular mapping of pixel location to a given radiance direction is straightforward. To check whether this is done properly we determine the calibration constant K in both air and water. If they are the same, then the instrument is set up properly. Before and after each deployment we do the angular calibration to help determine if any changes have happened in the optics. A typical example is shown below in Figure 3, for an in-water calibration. The K derived from this graph was 0.469 ±0.0038. The r^2 for this regression was 0.9995. One can see that the mapping is indeed a linear relationship.

The series of angular calibrations for one of the NuRADS instruments is shown in Figure 4. In this graph the in-water calibrations are shown as circles, while the in-air calibrations are shown as crosses. As can be seen, the angular calibration is both very stable, and the difference between the air and water values are very small. In the later calibrations, only air or water were performed to check instrument stability.

Note that because of the fisheye projection, the solid angle represented by each pixel varies, depending on nadir angle. The equation relating the solid angle represented by each pixel is:

$$\text{Solid angle} = K\,\pi/180\,\sin(\theta)/r$$

So that at 10 degree nadir angle, each pixel represents 0.3 millisteradian, while at 70 degrees the pixel area represents 0.2 millisteradian.

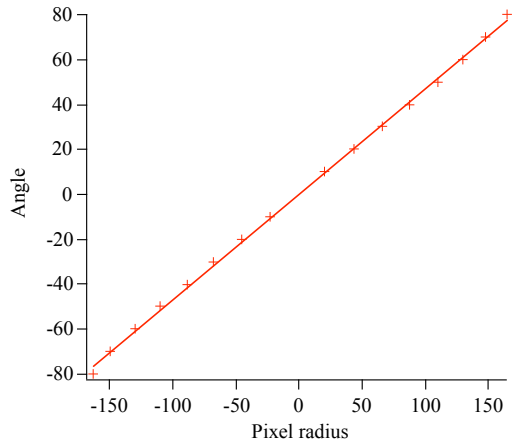

Figure 3) An example angular calibration. A small source is imaged by the camera, and a series of images is obtained as the camera is rotated. For each image, the source location in the image is determined and correlated with the rotation angle. The line is a linear least squares fit to the data.

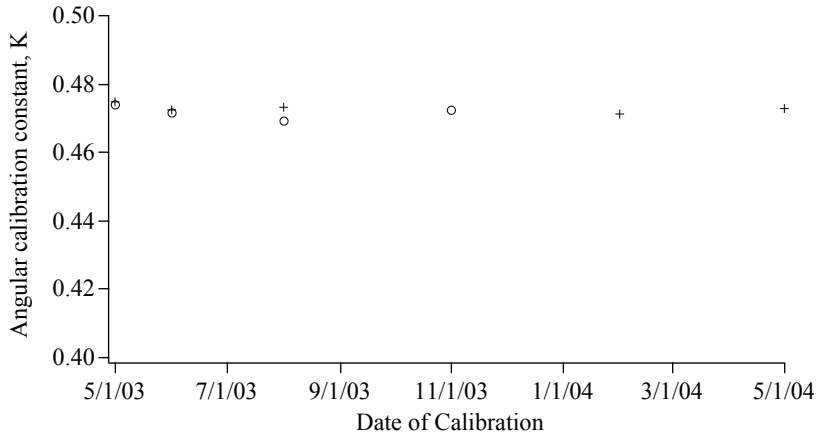

Figure 4) Angular calibration history for one of the NuRADS camera systems. In this graph the circles represent K for in-water calibrations while the crosses represent K for in-air calibrations.

D) Immersion calibration

The immersion calibration determines the difference in camera system response between measurements made in-air versus those in-water. For radiometers with flat windows this is caused by both the difference between air-glass and water-glass transmission, along with the index of refraction (n^2) effect between air (inside the instrument) and water (outside). With the fisheye system, and the hemispherical window, there is another effect which offsets this n^2 refraction effect. In essence the apparent aperture size of the system varies whether it is in-water or in-air. Hence, we must do a calibration to determine the immersion factor. The calibration is done in the following manner. The instrument is

placed, dry, in a barrel and a reflectance plaque is suspended above this barrel at 45 degrees to the vertical. The plaque is illuminated by a 1000W FEL lamp. Images of the plaque are obtained as the water level in the tank is raised above the level of the dome window. Several measurements are made with different water levels with the window submerged to determine the water attenuation. The average of a 20x20 pixel area, centered on the plaque, is obtained at each measurement point. The attenuation coefficient of the water is determined from the measurements at the different water levels, and is used to correct for attenuation effects. The apparent radiance that the plaque should have at the sensor (compensated for the air-water interface effects, and water attenuation) is used (Lwater and Lair), along with the pixel averages when the window was dry (#air) vs. wet (#water) to determine the immersion correction, *M*.

$$M = \text{Lwater}\ \ \#\text{air} / (\#\text{water}\ \text{Lair})$$

Typical immersion factors are on the order of 1.85.

E) Camera lens rolloff

The lens rolloff of the camera is measured in one of two ways. In each case, the total field of view of the camera is so large that there is not a uniform image to place in front of the system that will fill the entire field of view. Thus the rolloff data is acquired by sequentially imaging a stable source that fills a reasonable amount of the field of view and moving this source around the field of view. In the first method a reflectance plaque is the source, and data is acquired as this source moves in the field of view in two orthogonal axis. The two axis are done to check the azimuthal symmetry of the system. In the second method, a 1 m integrating sphere is used as the source, and the camera is placed as close to the source as possible, without imaging the integrating sphere source ports inside the sphere. This fills a significantly larger portion of the field of view of the system, and with several rotations, allows the entire system to be sampled. In either case a rolloff function is fit to the resulting data, vs angle. Below we show in Fig. 6 both the rolloff function of the NURADS system, along with the rolloff of the previous system, RADSII. The rolloff of the new system is much less severe than the old system. At 80°, the old rolloff factor was approximately 0.17, while the new system is on the order of 0.88. Thus the data from the new system is much more reliable at the larger angles.

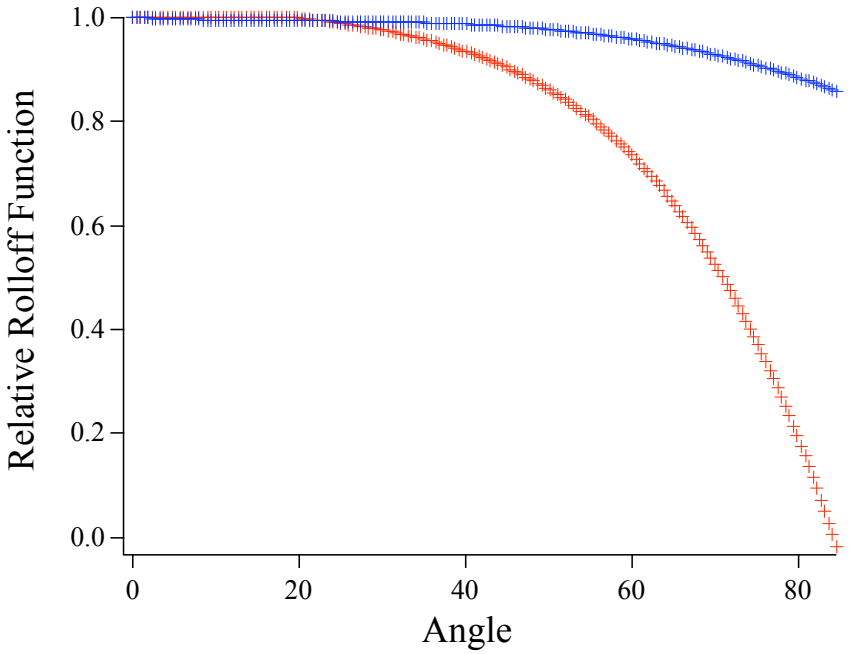

Figure 5) Rolloff functions for NuRADS (blue crosses) and for RADS-II (red crosses). As can be seen, the rolloff for the NuRADS system is much less severe than for the RADS-II system. At 80°, the rolloff is only 0.9 versus 0.2 for the older system.

F) Spectral calibration

The spectral calibration was performed by measuring the filter transmission of each filter in a spectro-photometer. Since the filters are only nominally 10 nm wide, there are no other sharp features in the system that would significantly effect the calibration.

Any, well blocked, 10 nm interference filter could be used; the characteristics of the filters we chose are shown in Table 1. In addition to the blocking provided with these filters, additional blocking was provided to reduce the infrared response (Schott glass BG18), and Wratten filters for some of the red bands to provide extra blocking for the blue light. Since this instrument is designed to primarily work measuring upwelling light at the surface, the blocking requirements for the blue light is less severe than a profiling instrument. After constructing the system, with the filter combinations to be used, tests

Table 1) Spectral characteristics of the current NuRADS configuration.

Filter	centroid	Full Width at Half Maximum
Filter 1	410.5 nm	9.6 nm
Filter 2	435.8 nm	10.8 nm
Filter 3	486.5 nm	10.8 nm
Filter 4	525.7 nm	10.0 nm
Filter 5	548.4 nm	15.3 nm
Filter 6	615.8 nm	9.8 nm

are also performed in the laboratory (imaging an FEL illuminated reflectance plaque) and in full sunlight (imaging a sunlight illuminated reflectance plaque). In these tests, additional filters are placed between the camera and the plaque, which either block the passband of the filter or some other spectral region. Measurements taken in this way can determine the residual out of band response. In these tests, our filter combinations were sufficiently blocked to keep total integrated out of band response to less than 1%.

G) Absolute calibration

Finally an absolute calibration is performed. We are currently using a radiance source made of a reflecting plaque (99% spectralon plaque) and a 1000W FEL lamp. The history of calibration for one of the instrument is shown in Figure 6. Note in this figure, Filter 5 has almost exactly the same numerical values as Filter 4, thus the symbol is hidden. With these calibration coefficients, and an integration time of 1 sec, each count represents on the order of 30 pW cm^{-2} nm^{-1} sr^{-1}. Full scale at 1 sec integration time is then 2 □W cm^{-2} nm^{-1} sr^{-1}.

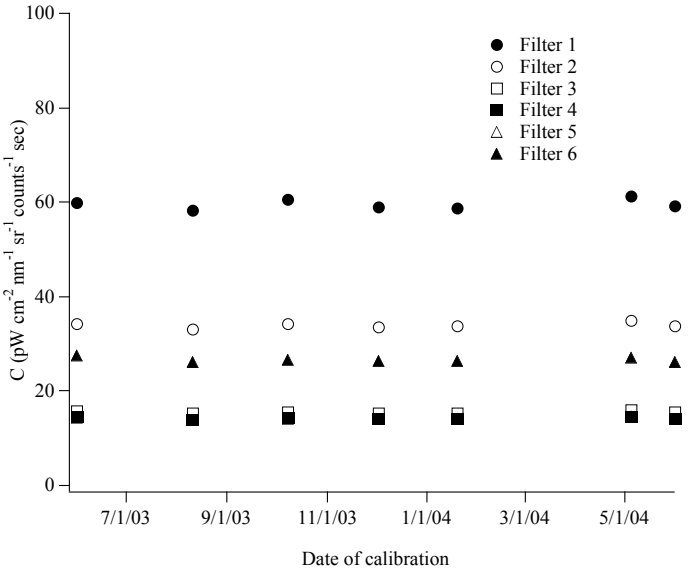

Figure 6) Calibration history of one of the NuRADS camera systems. As can be seen the absolute calibration is fairly stable over the instruments history.

4) Sample data

A) clear water case

The first set of sample data shown below was acquired on 10/22/2003 off of Honolulu, Hawaii. The solar zenith angle during these measurements was 38º (refracted in-water angle would be 27º). An image is shown for each wavelength. The water was very clear, with Chl approximately 0.1 mg/m^3.

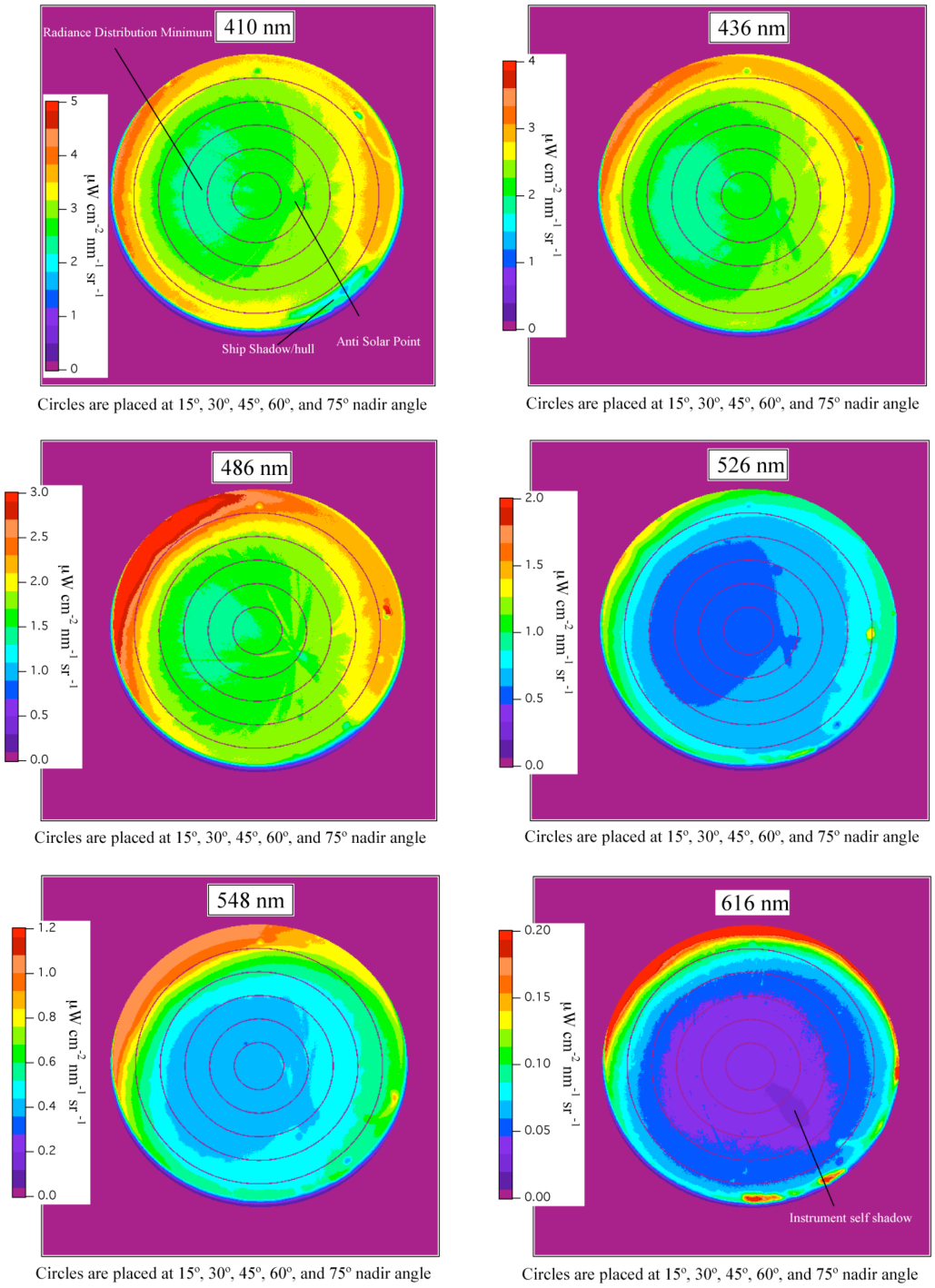

Figures 7) Upwelling radiance distribution images in clear water. Solar zenith angle is 38 degrees in air. At very large nadir angles, at the shorter wavelengths, the ship shadow or hull is evident and is labeled in one of the graphs At the reddest wavelength the direct instrument self shadow is quite evident and is labeled in the graph.

In these clear water images several things are evident. The first feature is that the minimum in the radiance distribution is actually on the sun side of the nadir, not on the

anti-solar side. While it is not as obvious in these false color images as it is in the grey scale images, the anti-solar point is evident as the point where the bright refracted rays converge. The anti-solar point is also evident in the longer wavelength (red) images, as the place where the instrument self shadow is evident, however since the instrument is a cylinder extending upwards from the bottom (where the measurement is made) the shadow actually extends upwards from the anti solar point. In all the shorter wavelength images, even though the instrument is approximately 30 m or more from the ship, the ship hull is evident on the horizon. Finally, while the radiance distribution is not isotropic, the range of values from nadir to the horizon is limited to a factor of 3 or less.

Two convenient simplifications, describing the shape of the upwelling radiance distribution, are the average cosine of the upwelling radiance distribution (μ_u) and Q_u, the ratio of the upwelling nadir radiance and the upwelling irradiance.

$$\mu_u = E_u/Eo_u$$

$$Q_u = L_u/E_u.$$

For an isotropic radiance distribution, Q_u would be equal to π and μ_u would be equal to 0.5. Table 2 shows Q_u and μ_u calculated from the images shown. As can be seen Q_u is slightly higher than π, as reflected in the images by the brightening in radiance towards the horizon. μ_u is slightly less than 0.5. The variation in these factors reflects the variation in the pure water absorption, with Q_u increasing towards the longer, red, more absorbed wavelengths.

Table 2) Q_u, μ_u, and L_u for the clear water radiance distributions.

Wavelength	Q_u	μ_u	L_u (μW cm^{-2} nm^{-1} sr^{-1})
410 nm	3.43	0.483	2.59
436 nm	3.35	0.481	2.11
486 nm	3.57	0.467	1.51
526 nm	3.49	0.457	0.569
548 nm	3.62	0.442	0.406
616 nm	3.96	0.382	0.039

Also note that L_u decreases from the blue to the red reflecting the obvious blue color of the water.

B) Turbid water case

The next example is taken from a turbid water case 2 data set. This data was obtained in the Chesapeake Bay on 5/19/03. The solar zenith angle (in air) was 33 degrees.

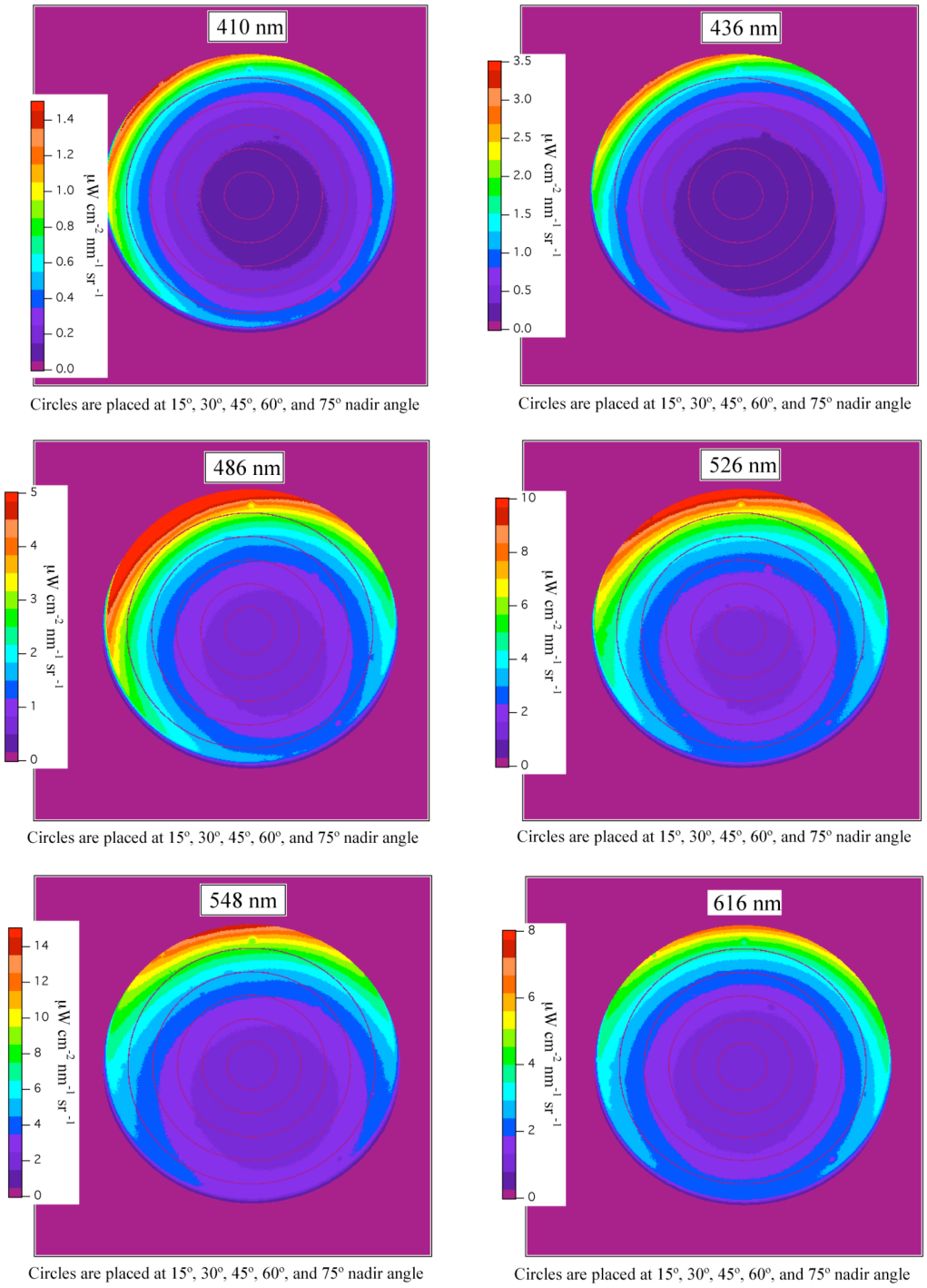

Figures 8) Upwelling radiance distribution images in turbid water. Solar zenith angle was 33 degrees in air. Because of the higher attenuation, the ship shadow is not evident (instrument 30m from ship). Note that there is a lot more variation in the upwelling radiance distribution from nadir to the horizon.

In these turbid case 2 waters, the radiance distribution has a lot more variation from nadir to the horizon. This is reflected in the Q_u and η_u factors shown in Table 3. The spectral

variation of the parameters, and the underlying radiance distribution, reflects the influence of dissolved organic material in these turbid waters, case 2 waters. In particular, the increased absorption at the lower wavelengths causes Q_u to be higher, and η_u to be lower than in the clear water case. As the wavelength increases, total absorption decreases, and Q_u decreases. This continues until 616 nm, where the water absorption becomes significant and once again Q_u increases.

Table 3) Q_u, η_u, and L_u for the turbid water radiance distributions.

Wavelength	Q_u	η_u	L_u
410 nm	6.66	0.345	0.103
436 nm	6.14	0.347	0.218
486 nm	5.64	0.369	0.660
526 nm	5.10	0.391	1.49
548 nm	4.95	0.398	1.96
616 nm	5.27	0.388`	0.939

It can be seen that, as expected in this turbid coastal water, the maximum upwelling nadir radiance is in the green, with little light coming out at the blue wavelengths. Also note the significant amount of nadir radiance at the red wavelength.

5) Conclusion

This instrument represents a significant advance in the measurement of the upwelling radiance distribution. The instrument has already been used during several cruises in Hawaii (clear water), the Chesapeake Bay (turbid coastal water), and in the Mediterranean during the recent BOUSELLE cruise. It will be used to improve the BRDF models for remote sensing, and help constrain backscattering phase functions in models.

6) Acknowledgements

This work was supported by the Ocean Optics program at the Office of Naval Research and NASA.

7) References

Aas, E., and N. K. Hojerslev. 1999. Analysis of underwater radiance distribution observations: apparent optical properties and analytical functions describing the angular radiance distributions. J. Geophys. Res. **104**: 8015 - 8024.

Doyle, J. P., and K. J. Voss. 2000. 3D Instrument Self-Shading effects on in-water multi-directional radiance measurements. Ocean Optics XV, Monaco, October 16-20.

Helliwell, W. S., G. N. Sullivan, B. Macdonald, and K. J. Voss. 1990. A finite-difference discrete-ordinate solution to the three dimensional radiative transfer equation. Transport Theory and Statistical Physics, **19**: 333-356.

Smith, R. C., R. W. Austin and J. E. Tyler. 1970. An oceanographic radiance distribution camera system. Appl. Opt. **9**: 2015-2022.

Tyler, J.E. 1960. Radiance distribution as a function of depth in an underwater environment. Bull. Scripps Inst. Oceanogr. **7**: 363-41.

Voss, K. J. 1989. Electro-optic camera system for measurement of the underwater radiance distribution. Optical Engineering. **28**: 241-247.

Voss, K. J. and A. L. Chapin. 1992. Next generation in-water radiance distribution camera system. Proc. Soc. Photo-Optical Instrumentation Engineers, **1759**: 384 - 387.

Voss, K. J., C. D. Mobley, L. K. Sundman, J. Ivey, and C. Mazell. 2003. The spectral upwelling radiance distribution in optically shallow waters. Limnol. Oceanogr. **48**: 364 - 373.

Voss, K. J. and A. Morel. 2004. Bidirectional reflectance function for oceanic waters with varying chlorophyll concentrations: measurements versus predictions. Limnol. Oceanogr. Submitted, 6/04.

Voss, K. J., and G. Zibordi. 1989. Radiometric and geometric calibration of a spectral electro-optic "fisheye' camera radiance distribution system. J. Atmosph. and Ocean. Techn., **6**: 652-662.